Nanoscale

Accepted Manuscript

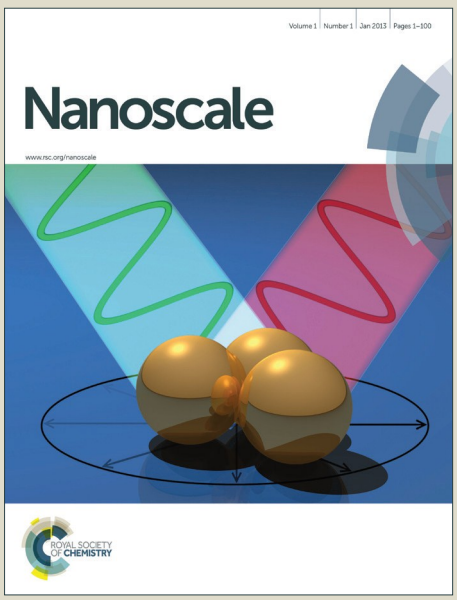

ROYAL SOCIETY OF CHEMISTRY

www.rsc.org/nanoscale

Cite this: DOI: 10.1039/c0xx00000x

www.rsc.org/xxxxxx

ARTICLE TYPE

Micro-nanostructured CuO/C spheres as high-performance anode material for Na-ion batteries

Yanying Lu, Ning Zhang, Qing Zhao, Jing Liang and Jun Chen*

Received (in XXX, XXX) Xth XXXXXXXXX 20XX, Accepted Xth XXXXXXXXX 20XX

In this paper, we report on the synthesis of micro-nanostructured CuO/C spheres by an aerosol spray pyrolysis and their application as high-performance anode of sodium-ion batteries. Micro-nanostructured CuO/C spheres with different CuO contents were synthesized through an aerosol spray pyrolysis with adjusting the ratio of reactants and heat-treated with oxidation process. The as-prepared CuO/C spheres show uniformly spherical morphology, in which CuO nanoparticles (~10 nm) are homogeneously embedded in carbon matrix (denoted as 10-CuO/C). The electrochemical performance of 10-CuO/C with carbon weight of 44% was evaluated as anode material for Na-ion batteries. It can deliver a capacity of 402 mAh g^{-1} after 600 cycles at a current density of 200 mA g^{-1}. Furthermore, a capacity of 304 mAh g^{-1} was obtained at a high current density of 2000 mA g^{-1}. The superior electrochemical performance of the micro-nanostructured CuO/C spheres attributes to the enhancement of electronic conductivity of the nanocomposite and the accommodation of the volume variation of CuO/C during charge/discharge cycling.

Introduction

Room-temperature rechargeable Na-ion batteries (NIBs) have been considered as potential alternatives for future energy-storage application because of the abundance and low cost of sodium sources.[1-5] However, Na ion (0.106 nm) has larger radius compared with Li ion (0.076 nm), leading to large volume expansion and sluggish kinetics during cycling. This results in the difficulty to identify stable electrode materials, especially for the anode materials,[6] with rapid and reversible Na ion insertion and extraction.[7] As a commercial anode material for Li-ion batteries, graphite is not a suitable candidate for NIBs because the interlayer distance of graphite is too small to accommodate Na ion.[8-10] Hence, it is urgent to develop other anodes in order to achieve improved electrochemical performance of NIBs.

Recently, efforts have been tried to find suitable anodes for NIBs.[11-13] Among the known anodes, transition metal oxides (M_xO_y) (M=Co, Ni, Cu, Fe, Mo) are considered as one of the best choices owing to their high theoretical capacity.[14-16] In particular, cupric oxide (CuO) has attracted large attention because of its abundance distribution, low-cost, and high safety.[17-19] However, similarly with the others metal oxides, practical application is still hindered by the poor conductivity and large volume expansion during charge/discharge processes since this leads to a large capacity fade and poor rate performance.[20] To solve these problems, recent reports have been tried to build stable nanostructured anodes to buffer the large volume variation.[21-24] For example, sheet-like CuO films on Cu substrate [25] have been fabricated by a corrosion process with a capacity of 100 mAh g^{-1} after 40 cycles at 200 mA g^{-1}. The porous CuO nanowires synthesized by precipitation method have been obtained by our group[26] with a capacity of 303 mAh g^{-1} after 50 cycles at 50 mA g^{-1}. Zhang's group [27] reported the preparation of binder-free porous CuO arrays by engraving copper foils in situ, which exhibited a reversible capacity of 542 mAh g^{-1} after 30 cycles at 50 mA g^{-1}. These studies show that nanostructures can improve the electrochemical performance of CuO in NIBs.[28] However, long-term cyclability and high-rate capability are still difficult to meet the commercial requirements. The nano-morphologies need to be stabilized by matrix for long cycling consideration.[29, 30] In addition, the poor electronic conductivity is to be improved. Building a carbon matrix to hold nanostructured CuO could be a selection.[31] The carbon matrix can enhance the electronic conductivity and act as a buffer to alleviate the effect of volume change during cycling.[32] However, to our knowledge, report on CuO/C composites for NIBs is limited. It is noted that methods to prepare carbon-contained composites have been widely proposed in LIBs and some electrodes in NIBs.[33-35] Among them, the aerosol spray pyrolysis, which mainly focuses on the synthesis of various carbon-contained materials, has attracted a great attention because of its fast and facile process.[36-38] Particularly, thus method usually obtains composites of host material with small nanoparticles and substrate carbon frameworks that can effectively benefit the electrochemical performance.

Herein, we report on the synthesis of micro-nanostructured CuO/C spheres and their application as high-performance anode materials of sodium-ion batteries. The CuO/C spheres have been synthesized by an aerosol spray pyrolysis associated with oxidation process. The CuO/C nanocomposite has spherical morphology with the uniform distribution of CuO nanoparticles (diameter of ~ 10 nm) in the carbon matrix. Moreover, the sample of 10-CuO/C with carbon weight of 44% exhibits outstanding cyclability and high-rate performance. After 600 cycles, it can keep a capacity of 402 mAh g^{-1} at a current density of 200 mA g^{-1}. Additionally, a capacity of 304 mAh g^{-1} was delivered at a high current density of 2000 mA g^{-1}. The nanosized CuO guarantees the high electrochemical reactivity, while the porous carbon sphere improves the conductivity and stabilizes the anode

structure. These factors synergetically contribute to the excellent electrochemical properties.

Experimental

Synthesis of micro-nanostructured CuO/C spheres with different CuO sizes. The CuO/C nanocomposite was synthesized using an aerosol spray pyrolysis approach followed with oxidation process. As illustrated in Scheme 1, the synthetic process mainly involves two steps. First, the synthesis of Cu-Cu_xO/C; 23.5 g resorcinol and 25 mL of formaldehyde were polymerized to form resorcinol formaldehyde (RF) resin solution at room temperature. Then, the prepared RF resin solution and 2.55 g copper nitrate trihydrate ($Cu(NO_3)_2 \cdot 3H_2O$) were dissolved in 275 mL of ethanol. This precursor solution was atomized with a firm output atomizer (Model 3076, TSI, Inc.) under argon atmosphere at a pressure of 0.18 MPa. The produced aerosol droplets were passed through a 2.54 cm (ID) × 80 cm (L) quartz tube within a tube furnace set at 800 °C. The dwell time of the aerosol droplets in the tube furnace was roughly 1−2 s to facilitate the aerosols evaporation and self-assembly. A short collection device (2.5 cm (ID) × 2.0 cm (L)) was placed at the end of the quartz tube to collect the composite. Second, the obtained Cu-Cu_xO/C product was heated at 260 °C for 3h in air to get the CuO/C nanocomposites with CuO particle size of about 10 nm (denoted as 10-CuO/C). For comparison, the CuO/C composite with the CuO size of 40 nm was prepared by the same process except that the precursor content of $Cu(NO_3)_2 \cdot 3H_2O$ was added to 5.11 g (labeled as 40-CuO/C). Pure CuO particles were also prepared in the same steps without RF resin solution added into the precursor solution.

Material characterizations. The phase structure and purity of the samples were evaluated by XRD recorded on a Rigaku MiniFlex600 diffractometer using Cu Kα radiation in the 2θ range of 10−80 °. Field-emission scanning electron microscopy (SEM, JEOL JSM7500F) and transmission electron microscopy (TEM, Philips Tecnai-F20) images were taken to further characterize the products. The carbon content in the CuO/C nanocomposites were determined by Thermogravimetric analysis (TGA) on a TG-DSC analyzer (NETZSCH, STA 449 F3) in air with a heating rate of 5 °C min^{-1} from 25 °C to 600 °C. Raman spectra were collected using a confocal Raman microscope (DXR, Thermo Fisher Scientific) from an argon ion laser with excitation at 532nm.

Electrochemical measurements. The electrodes of 10-CuO/C, 40-CuO/C and pure CuO particles were prepared from a mixture of the active material with polyvinylidene fluoride (PVdF) and carbon black (Super−P) (weight ratio: 80:10:10) mixed in N-methyl pyrrolidinone (NMP) to form homogeneous slurry. the carbon in our materials of 10-CuO/C and 40-CuO/C, we added carbon black to enhance the electronic conductivity. The obtained slurry was pasted onto Cu foil and dried in a vacuum oven at 110 °C for 10 h. The electrochemical performance of the electrodes was evaluated using CR2032 coin−type cells assembled in an argon−filled glove box. Na metal was used as the counter and reference electrode. Celgard 2320 was used as the separator. 1 M $NaPF_6$ in a mixture of dimethyl carbonate (DMC), ethylene carbonate (EC) (1:1 in volume) and fluoroethylene (FEC) (5 %) were used as the electrolyte. Galvanostatic charge/diacharge tests at different rates were conducted on a LAND−CT2001A battery instrument in the voltage range of 0.01− 3.0 V. Cyclic voltammetry (CV) tests scanned at 0.1mV s^{-1} between 0 and 3 V were recorded using a Parstat 263A electrochemical workstation (AMTECT Company). All the specific capacity values in this paper were calculated on the mass of CuO. Electrochemical impedance spectroscopy (EIS) measurements were carried out using Parstat 2273 electrochemical workstation over a frequency range from 100 mHz to 100 kHz.

Result and discussion

Scheme 1 illustrates the aerosol spray pyrolysis apparatus and the preparation process with the formation of micro-nanostructured CuO/C spheres through the aerosol pyrolysis (step 1) and the subsequent oxidation process (step 2). In step 1, the aerosol droplets (contained Cu ions and RF resin) were continuously sprayed through the atomizer under argon atmosphere. The precursor droplets passed through a heating zone (800 °C) and converted into composite particles which contained Cu-Cu_xO and carbon (RF resin was carbonized in this high temperature). The Cu-Cu_xO/C composite was collected at the end of the furnance tube (XRD showed in Fig. S1). In step 2, the composite was oxidized in Muffle furnace to finish the conversion from Cu-Cu_xO/C to CuO/C.

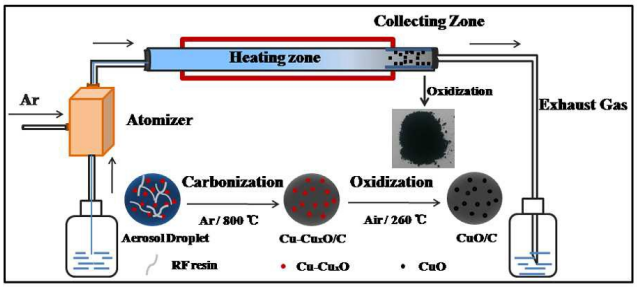

Scheme. 1 Schematic illustration for aerosol spray pyrolysis apparatus and the formation process of micro-nanostructured CuO/C spheres.

Fig. 1(a) shows the XRD patterns of the as-prepared nanocomposites. All the peaks of these samples can be indexed to a C2/c space group of monoclinic crystal system CuO (JCPDS no. 45-0937). No peaks of Cu or Cu_2O are observed, indicating the high purity of the products. The broad peak of carbon located at around 24 degree is also found in the samples of 10-CuO/C (the red line) and 40-CuO/C (the green line). Raman spectra were applied to further characterize the samples. As presented in Fig. 1(b), all of the as-prepared samples show three typical CuO peaks at about 298 cm^{-1}, 347 cm^{-1} and 630 cm^{-1}.[39] In addition, two broad peaks which are located at 1338 cm^{-1} and 1590 cm^{-1} can be assigned to the typical D and G bands of carbon,[40] respectively. TGA reveals that the CuO content of 10-CuO/C and 40-CuO/C are approximately 44 % and 70 % (Fig. S2), separately. Moreover, according to the result of nitrogen (N_2) absorption-desorption isotherms, the samples of 10-CuO/C and 40-CuO/C show a specific surface area of 262 m^2 g^{-1} and 122 m^2 g^{-1}, respectively (Fig. S3).

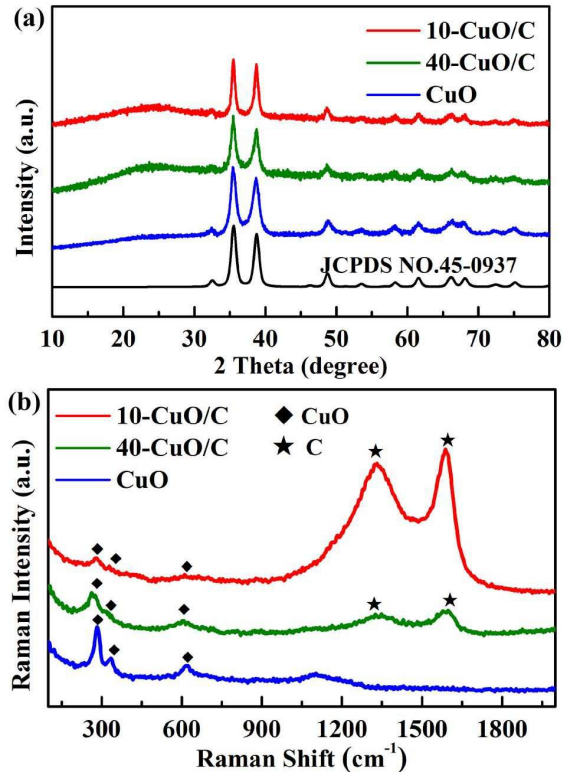

Fig. 1 (a) XRD patterns of 10-CuO/C, 40-CuO/C, pure CuO particles and standard card of CuO (JCPDS no. 45-0937), (b) Raman spectra of as-prepared 10-CuO/C, 40-CuO/C and pure CuO particles.

Fig. 2 displays the SEM and TEM images of 10-CuO/C and 40-CuO/C. As shown in Fig. 2(a), 10-CuO/C has uniformly spherical morphology with an average diameter of about 210 nm (Fig. S4). The TEM images of 10-CuO/C with different magnifications in Fig. 2(b-c) reveal that CuO (black dots) particles with the average size of approximately 10 nm are homogeneously embedded in the carbon framework (grey matrix). The HRTEM image of 10-CuO/C (top right corner of Fig. 2(c)) shows a set of parallel fringes with the space of 0.25 nm, corresponding to the (002) plane of crystalline CuO (JCPDS no. 45−0937). The TEM elemental mapping image of 10-CuO/C (Fig. 2(d)) shows the homogenous distribution of CuO within the nanocomposite. For comparison, 40-CuO/C has uneven shape (Fig. 2(e)). The reason is that the relative low ratio of carbon can not support enough spherical structure. The TEM images in Fig. 2(f-g) show the inner CuO particles of 40-CuO/C with the average size of about 40 nm. In addition, the SEM image of pure CuO particles which were sprayed without RF resin solution is showed in Fig. S5. Moreover, the carbon content of the composite can be controlled by adjusting the concentration of precursor solution. The proper ratio of precursor concentration in 10-CuO/C leads to the advantage of uniformly embedded CuO particles (~10 nm). The SEM and TEM images of CuO/C with different ratio of reactants are shown in Fig. S6.

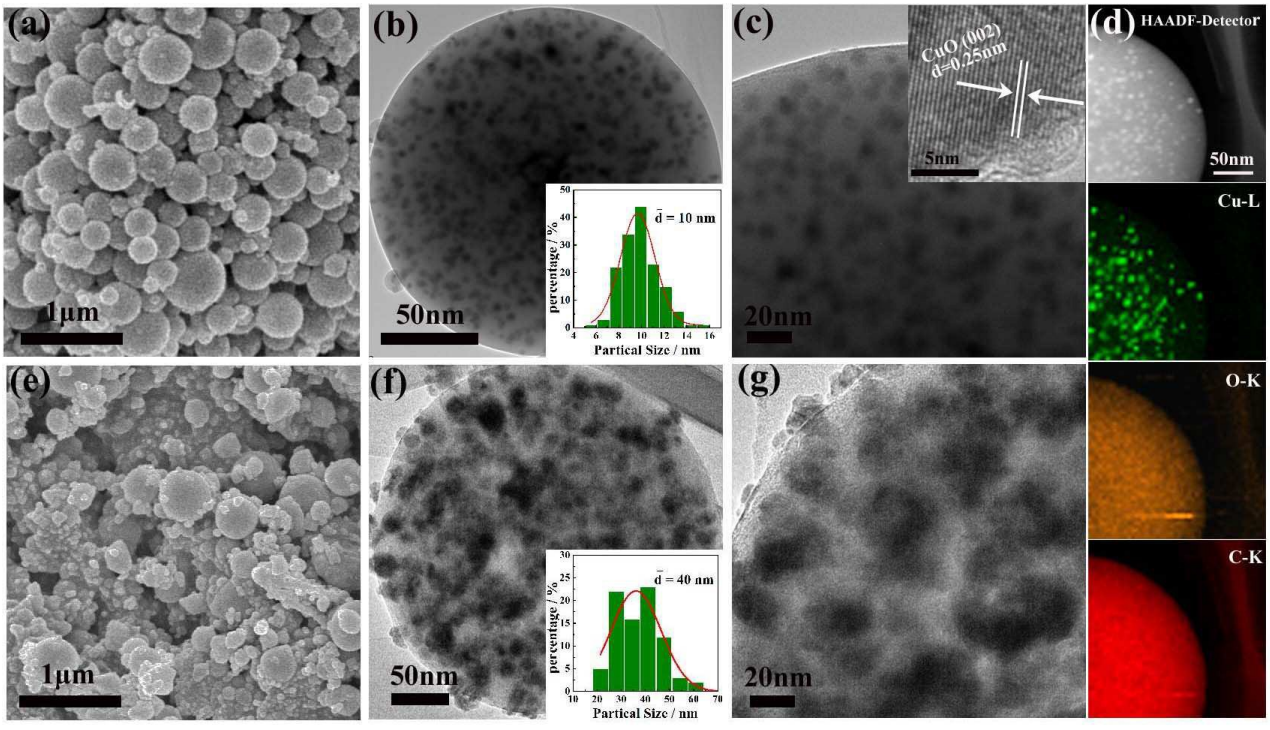

Fig. 2 (a) SEM image of 10-CuO/C, (b) TEM image of 10-CuO/C (the inset: corresponding particle size analysis of CuO), (c) TEM and HRTEM (top right corner) images of 10-CuO/C, (d) TEM (HAADF, Cu, O, C) elemental mapping images of 10-CuO/C, (e) SEM image of 40-CuO/C, (f) TEM image (the inset: corresponding particle size analysis of CuO) and (g) TEM images of 40-CuO/C.

The suitable architecture of 10-CuO/C inspires us to further study its electrode performance. Fig. 3(a-b) shows the charge/discharge curves of 10-CuO/C and 40-CuO/C at a current density of 50 mA g^{-1} between 0.01 and 3.0 V. In the first cycle,

the two samples show similar curves. The discharge capacities of 10-CuO/C and 40-CuO/C are 801 and 770 mAh g^{-1}, while the charge capacities are 660 mAh g^{-1} and 606 mAh g^{-1}, respectively. The initial capacity loss could be mainly attributed to the formation of SEI layer.[41] In the subsequent cycles, compared with 40-CuO/C, the charge and discharge curves of 10-CuO/C overlap well, indicating the high reversibility of the material. In addition, the cyclic voltammogram (CV) of 10-CuO/C and 40-CuO/C are scanned at a rate of 0.2 mV/s between 0.01 V and 3.0 V. The plateaus observed in both charge and discharge curves accord well with the CV curves, as illustrated in Fig. 3(c-d). During the initial discharge cycle, a broad peak at 1.03 V attributes to the decomposition of the organic electrolyte and the formation of SEI layer.[27] In the subsequence cycles, the reduction peaks at 1.83, 0.54, and 0.12 V during the discharging process involve three reversible electrochemical reactions: the formation of $Cu^{II}_{1-x}Cu^{I}_{x}O_{1-x/2}$, the generation of Cu_2O phase, further reduction of Cu_2O phase into Cu and Na_2O, respectively.[42, 43] The corresponding equations are expressed[26]:

$CuO + x\,Na^+ + x\,e^- \rightarrow Cu^{II}_{1-x}Cu^{I}_{x}O_{1-x/2} + x/2\,Na_2O$ (1)

$2\,Cu^{II}_{1-x}Cu^{I}_{x}O_{1-x/2} + (2\text{-}2x)\,Na^+ + (2\text{–}2x)\,e^- \rightarrow Cu_2O + (1\text{–}x)\,Na_2O$ (2)

$Cu_2O + 2\,Na^+ + 2\,e^- \rightarrow 2\,Cu + Na_2O$ (3)

Meanwhile, in the charging process, the oxidation peak at 1.3 V is corresponding to the process $2Cu + Na_2O \rightarrow Cu_2O + 2Na$. The peak at 2.19 V attributes to the oxidation of Cu_2O phase into CuO. Further *ex-situ* XRD patterns observed at six designated potentials accord well with the products discussed above (Fig. S7). This confirms the conversion mechanism of CuO/C material during the charge/discharge processes. Notably, after the first cycle, the subsequent CV curves of 10-CuO/C are very similar compared with 40-CuO/C, indicating the stable electrochemical reaction.[44]

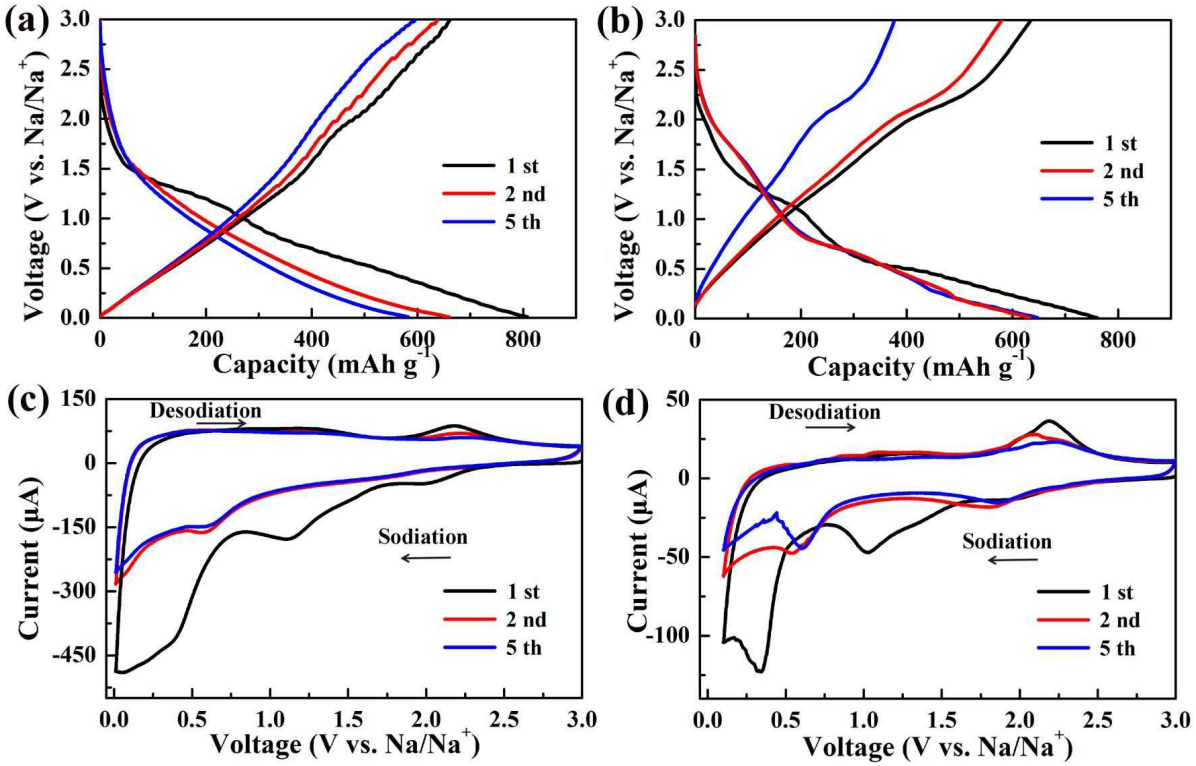

Fig. 3 Charge/discharge curves of (a) 10-CuO/C and (b) 40- CuO/C at a current density of 50 mA g^{-1}, cyclic voltammograms of (c) 10-CuO/C and (d) 40-CuO/C between 0.01 V and 3.0 V at the rate of 0.2 mV/s .

The cycling stability of 10-CuO/C, 40-CuO/C, and pure CuO particles at a current density of 50 mA g^{-1} are shown in Fig. 4a. The discharge capacity of 10-CuO/C (red points in Fig. 4a) maintains well with the increasing of cycling. It delivers a discharge capacity of 458 mAh g^{-1} after 50 cycles and remains 426 mAh g^{-1} after 100 cycles. As comparison, 40-CuO/C (green points in Fig. 4(a)) displays a discharge capacity of 217 mAh g^{-1} after 50 cycles, which is only half of the capacity of 10-CuO/C. Furthermore, pure CuO particles (black points in Fig. 4(a)) show a discharge capacity of 150 mAh g^{-1} after 15 cycles. The high capacity retention of 10-CuO/C indicates the sufficient utilization of CuO through the whole spherical carbon. To further investigate the superior cycling performance of 10-CuO/C, TEM analysis has been used to observe the morphological change of 10-CuO/C and 40-CuO/C after 50 cycles (after charge, about 3.0 V) at 50 mAh g^{-1}. The micro-nanostructured 10-CuO/C spheres (Fig. 4(b)) in general keep their original spherical shape. It can be seen that CuO particles with the embedded structure maintained well, without the aggregation of particles. This ensures its outstanding cycling performance. However, the sample of 40-CuO/C suffers from severe structure and morphology deformation after cycling, as illustrated in Fig. 4(c). The large

volume variation of CuO and the destruction of carbon framework result in the worse cycling stability.

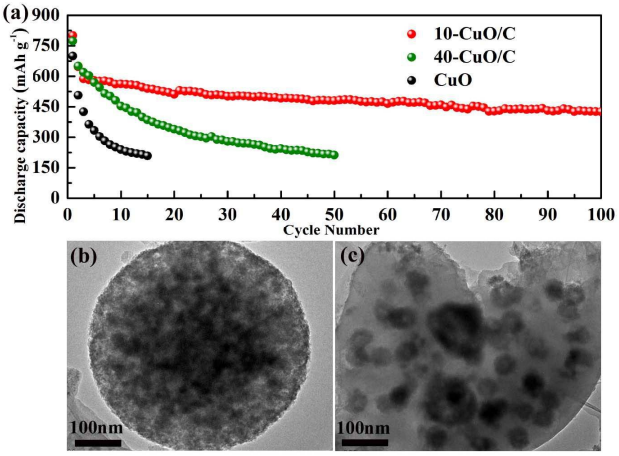

Fig. 4 (a) Cycling performances of the as-prepared samples at a current density of 50mA g^{-1}, (b) TEM image of 10-CuO/C after 50 charge/discharge cycles, (c) TEM image of 40-CuO/C after 50 charge/discharge cycles.

The sample of 10-CuO/C nanocomposite also exhibits excellent rate performance, as displayed in Fig. 5(a). It sustains a discharge capacity of 304 mAh g^{-1} even at a current density of 2000 mA g^{-1}. Once the current density returns to 50 mA g^{-1} after high rate cycling, the capacity still remains 512 mAh g^{-1}. In contrast, the sample of 40-CuO/C shows the discharge capacity of 110 mAh g^{-1} at 2000 mA g^{-1} with poor rate performance. The discharge capacities of 10-CuO/C and 40-CuO/C at different current densities are summarized in Table S1. To further understand the difference in electrochemical performance among 10-CuO/C, 40-CuO/C, and pure CuO particles, the electrochemical impedance spectroscopy (EIS) was conducted on the three fresh electrodes (Fig. 5(b)). The impedance spectra all contain a semicircle at the high-frequency and a straight line at the low-frequency, corresponding to the charge transfer resistance (R_{ct}) and a semiinfinite Warburg diffusion (Z_w) process, respectively. Obviously, the diameter of 10-CuO/C electrode in the high-frequency region is rather smaller than that of 40-CuO/C and pure CuO particles. This shows that 10-CuO/C nanocomposite possesses lower charge transfer resistance with rapid electron transport during insertion and extraction. The smaller resistance contributes to the outstanding rate performance of 10-CuO/C. Fig. 5(c) shows the high current density (200 mA g^{-1}) cycling performance and the coulombic efficiency of 10-CuO/C. In addition, the carbon matrix shows a discharge capacity of 41 mAh g^{-1} after 100 cycles at 200 mAh g^{-1}(Fig. S8). Even after 600 cycles, the 10-CuO/C nanocomposite still retains a capacity of 402 mAh g^{-1} with a coulombic efficiency of 99%. This result is superior to those previously reported for CuO materials.[26, 27, 45] This much improved cycling stability of 10-CuO/C is owing to its robust micro-nano architecture. First, the electronic conductivity of the CuO/C nanocomposite is enhanced in comparison with that of CuO. Second, the uniformly embedded CuO nanoparticles in the carbon framework can accommodate the volume variation of CuO/C during cycling. This effectively alleviates the absolute stress/strain of the nanocomposite electrode during repeated charge/discharge processes.[46]

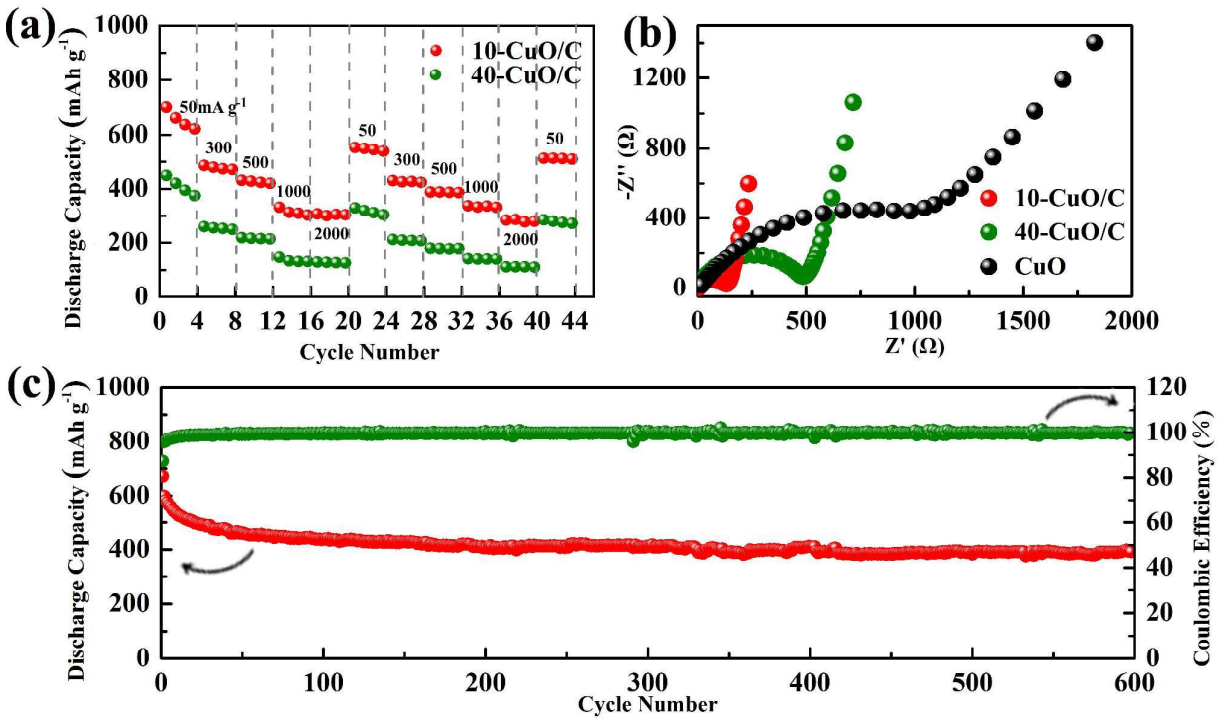

Cite this: DOI: 10.1039/c0xx00000x

www.rsc.org/xxxxxx

ARTICLE TYPE

Fig. 5 (a) Rate capability of 10-CuO/C and 40-CuO/C at different current densities, (b) EIS of 10-CuO/C, 40-CuO/C and pure CuO particles, (c) Cycling performance of 10-CuO/C at a current density of 200 mA g^{-1}

Conclusions

The micro-nanostructured CuO/C spheres have been synthesized by a scalable, simple, and low-cost aerosol spray pyrolysis followed with thermal oxidation in air. The selected nanocomposite shows a micro-nano structure with the uniform distribution of spherical CuO nanoparticles (diameter of ~10 nm) in carbon matrix. The CuO/C nanocomposite with such a micro-nano structure exhibits stable cycling performance and superior rate capability. It can deliver a capacity of 402 mAh g^{-1} after 600 cycles at a current density of 200 mA g^{-1}. Even at a high current density of 2000 mA g^{-1}, the capacity still maintains 304 mAh g^{-1}. These excellent electrochemical performances are attributed to the robust micro-nano architecture which can accommodate the volume variation of CuO/C during charge/discharge cycling. Thus, spherical CuO/C nanocomposite is potential in the application as the high-performance anode materials for NIBs.

Acknowledgements

This work was supported by Programs of National 973 (2011CB935900), NSFC (51231003, and 21322101), and MOE (B12015 and IRT13R30).

Notes and references

Key Laboratory of Advanced Energy Materials Chemistry (Ministry of Education), Collaborative Innovation Center of Chemical Science and Engineering, Nankai University, Tianjin 300071, China; Fax: 86-22-23509571; Tel: 86-22-23206808. E-mail: chenabc@nankai.edu.cn

† Electronic Supplementary Information (ESI) available: XRD pattern of Cu-Cu_xO. TGA curves of 10-CuO/C and 40-CuO/C. Particle size analysis of 10-CuO/C. SEM images of pure CuO particles. SEM and TEM images of CuO/C composites (different CuO content). Charge/discharge curves and cycling performance of the pyrolyzing carbon at 200 mA g^{-1}. The discharge capacities of 10-CuO/C and 40-CuO/C at different current densities.

1. S. W. Kim, D. H. Seo, X. Ma, G. Ceder and K. Kang, *Adv. Energy Mater.*, 2012, **2**, 710-721.
2. S. W. Wang, L. J. Wang, Z. Q. Zhu, Z. Hu, Q. Zhao and J. Chen, *Angew. Chem. Int. Ed.*, 2014, **53**, 5892-5896.
3. M. D. Slater, D. Kim, E. Lee and C. S. Johnson, *Adv. Funct. Mater.*, 2013, **23**, 947-958.
4. N. Yabuuchi, M. Kajiyama, J. Iwatate, H. Nishikawa, S. Hitomi, R. Okuyama, R. Usui, Y. Yamada and S. Komaba, *Nat. Mater.*, 2012, **11**, 512-517.
5. W. C. Duan, Z. Q. Zhu, H. Li, Z. Hu, K. Zhang, F. Y. Cheng and J. Chen, *J. Mater. Chem. A*, 2014, **2**, 8668-8675.
6. W. Li, S. L. Chou, J. Z. Wang, J. H. Kim, H. K. Liu and S. X. Dou, *Adv. Mater.*, 2014, **26**, 4037-4042.
7. Y. C. Liu, N. Zhang, L. F. Jiao, Z. L. Tao and J. Chen, *Adv. Funct. Mater.*, 2014, DOI: 10.1002/adfm.201402943.
8. B. Jache and P. Adelhelm, *Angew. Chem. Int. Ed.*, 2014, **53**, 10169-10173.
9. J. Sangster, *J. Phase Equilib. Diff.*, 2007, **28**, 571-579.
10. Y. L. Cao, L. F. Xiao, M. L. Sushko, W. Wang, B. Schwenzer, J. Xiao, Z. M. Nie, L. V. Saraf, Z. G. Yang and J. Liu, *Nano Lett.*, 2012, **12**, 3783-3787.
11. W. Wang, C. J. Yu, Z. S. Lin, J. G. Hou, H. M. Zhu and S. Q. Jiao, *Nanoscale*, 2013, **5**, 594-599.
12. Z. Hu, L. X. Wang, K. Zhang, J. B. Wang, F. Y. Cheng, Z. L. Tao and J. Chen, *Angew. Chem. Int. Ed.*, 2014, **53**, 12794-12798..
13. W. H. Ryu, J. W. Jung, K. S. Park, S. J. Kim and I. D. Kim, *Nanoscale*, 2014, **6**, 10975-10981.
14. S. L. Chou, J. Z. Wang, D. Wexler, K. Konstantinov, C. Zhong, H. K. Liu and S. X. Dou, *J. Mater. Chem. A*, 2010, **20**, 2092-2098.
15. J. Chen, L. N. Xu, W. Y. Li and X. L. Gou, *Adv. Mater.*, 2005, **17**, 582-586.
16. W. Y. Li, L. N. Xu and J. Chen, *Adv. Funct. Mater.*, 2005, **15**, 851-857.
17. L. L. Wang, W. Cheng, H. X. Gong, C. H. Wang, D. K. Wang, K. B. Tang and Y. T. Qian, *J. Mater. Chem.*, 2012, **22**, 11297-11302.
18. Y. M. Li, J. Liang, Z. L. Tao and J. Chen, *Mater. Res. Bull.*, 2008, **43**, 2380-2385.
19. J. Wang, Y. C. Liu, S. Y. Wang, X. T. Guo and Y. P. Liu, *J. Mater. Chem. A*, 2014, **2**, 1224-1229.
20. F. Y. Cheng and J. Chen, *J. Mater. Chem.*, 2011, **21**, 9841-9848.
21. J. Chen and F. Y. Cheng, *Acc. Chem. Res.*, 2009, **42**, 713-723.
22. J. H. Ju and K. S. Ryu, *J. Electrochem. Soc.*, 2011, **158**, A814-A817.
23. B. Peng and J. Chen, *Coord. Chem. Rev.*, 2009, **253**, 2805-2813.
24. O. Waser, M. Hess, A. Güntner, P. Novák and S. E. Pratsinis, *J. Power Sources*, 2013, **241**, 415-422.
25. Y. Liu, Y. Qiao, W. X. Zhang, P. Hu, C. J. Chen, Z. Li, L. X. Yuan, X. L. Hu and Y. H. Huang, *J. Alloy. Compd.*, 2014, **586**, 208-215.
26. L. J. Wang, K. Zhang, Z. Hu, W. C. Duan, F. Y. Cheng and J. Chen, *Nano Res.*, 2014, **7**, 199-208.
27. S. Yuan, X. L. Huang, D. L. Ma, H. G. Wang, F. Z. Meng and X. B. Zhang, *Adv. Mater.*, 2014, **26**, 2273-2279.
28. Q. Pan, H. Z. Jin, H. B. Wang and G. P. Yin, *Electrochim. Acta*, 2007, **53**, 951-956.
29. S. J. Peng, L. L. Li, H. B. Wu, S. Madhavi and X. W. Lou, *Adv. Energy Mater.*, 2014, **1401172**, 1-7.
30. W. C. Duan, Z. Hu, K. Zhang, F. Y. Cheng, Z. L. Tao and J. Chen, *Nanoscale*, 2013, **5**, 6485-6490.
31. C. B. Zhu, X. K. Mu, P. A. van Aken, Y. Yu and J. Maier, *Angew. Chem. Int. Ed.*, 2014, **53**, 2152-2156.

32. S. J. Peng, L. L. Li, S. G. Mhaisalkar, M. Srinivasan, S. Ramakrishna and Q. Y. Yan, *ChemSusChem.*, 2014, **7**, 2212-2220.
33. X. Zhou, Z. H. Dai, S. H. Liu, J. C. Bao and Y. G. Guo, *Adv. Mater.,* 2014, **26**, 3943-3949.
34. L. W. Ji, M. Gu, Y. Y. Shao, X. L. Li, M. H. Engelhard, B. W. Arey, W. Wang, Z. M. Nie, J. Xiao, C. M. Wang, J. G. Zhang and J. Liu, *Adv. Mater.*, 2014, **26**, 2901-2908.
35. Z. Q. Zhu, S. W. Wang, J. Du, Q. Jin, T. L. Zhang, F. Y. Cheng and J. Chen, *Nano Lett.*, 2014, **14**, 153-157.
36. X. L. Jia, Z. Chen, X. Cui, Y. T. Peng, X. L. Wang, G. Wang, F. Wei and Y. F. Lu, *ACS Nano*, 2012, **11**, 9911-9919.
37. N. Zhang, Q. Zhao, X. P. Han, J. G. Yang and J. Chen, *Nanoscale*, 2014, **6**, 2827-2832.
38. H. Sohn, M. L. Gordin, T. Xu, S. R. Chen, D. P. Lv, J. X. Song, A. Manivannan and D. H. Wang, *ACS Appl. Mater. Inter.*, 2014, **6**, 7596-7606.
39. H. F. Goldstein, D. S. Kim, P.Y. Yu, L.C. Bourne, *Phys. Rev. B*, 1990, **41**, 7192-7194.
40. Z. Q. Zhu, F. Y. Cheng and J. Chen, *J. Mater. Chem. A*, 2013, **1**, 9484-9490.
41. X. Wang, D. M. Tang, H. Q. Li, W. Yi, T. Y. Zhai, Y. Bando and D. Golberg, *Chem. Commun.*, 2012, **48**, 4812-4814.
42. C. K. Wu, M. Yin, S. O'Brien and J. T. Koberstein, *Chem. Mater*, 2006, **18**, 6054-6058.
43. L. Martin, H. Martinez, D. Poinot, B. Pecquenard and F. Le Cras, *J. Power Sources*, 2014, **248**, 861-873.
44. Y. H. Xu, G. Q. Jian, M. R. Zachariah and C. S. Wang, *J. Mater. Chem. A*, 2013, **1**, 15486-15490.
45. F. Klein, B. Jache, A. Bhide and P. Adelhelm, *Phys. Chem. Chem. Phys.,* 2013, **15**, 15876-15887.
46. N. Zhang, X. P. Han, Y. C. Liu, X. F. Hu, Q. Zhao and J. Chen, *Adv. Energy Mater.*, 2014, DOI: 10.1002/aenm.201401123.

TOC：

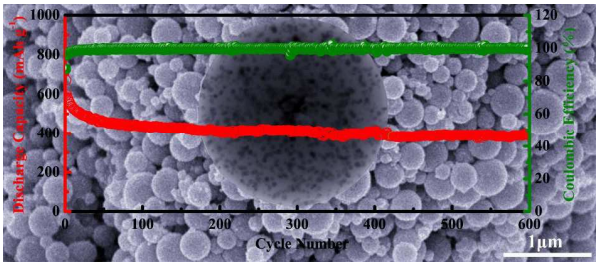

Micro-nanostructured CuO/C spheres, which were synthesized by an aerosol spray pyrolysis, show high performance as anode material for Na-ion batteries.